Ⓔ

A STARFISH PREPLANETARY NEBULA:[1] IRAS 19024+0044

RAGHVENDRA SAHAI,[2] CARMEN SÁNCHEZ CONTRERAS,[3] AND MARK MORRIS[4]

ABSTRACT

Using the *Hubble Space Telescope*, we have imaged the OH/IR star IRAS 19024+0044 (I19024) at 0.6, 0.8, 1.1, and 1.6 μm, as part of our surveys of candidate preplanetary nebulae. The images show a multipolar nebula of size $\sim3\farcs7\times2\farcs3$, with at least six elongated lobes emanating from the center of the nebula. Two of the lobes show limb-brightened tips having point-symmetric structure with respect to the expected location of the central star. The central region shows two dark bands southwest and northeast of a central shallow maximum that may be either two inclined dusty toroidal structures or the dense parts of a single wide, inhomogeneous, toroid. A very faint, surface brightness–limited, diffuse halo surrounds the lobes. Long-slit/echelle optical spectroscopy obtained at the Mount Palomar and Keck observatories shows a spatially compact source of Hα emission; the Hα line shows a strong, narrow, central core with very broad (±1000 km s^{-1}), weak wings, and a narrower blueshifted absorption feature signifying the presence of a ~100 km s^{-1} outflow. The spectrum is characterized by a strong, relatively featureless, continuum and lacks the strong forbidden emission lines characteristic of planetary nebulae, confirming that IRAS 19024 is a preplanetary nebula; the spectral type for the central star, although uncertain, is most likely early G. Interferometric observations of the CO $J = 1-0$ line emission with the Owens Valley Radio Interferometer show a marginally resolved molecular envelope (size $5\farcs5\times4\farcs4$) with an expansion velocity of 13 km s^{-1}, resulting from the asymptotic giant granch (AGB) progenitor's dense, slow wind. We derive a kinematic distance of 3.5 kpc to I19024, based on its radial velocity. The bolometric flux is 7.3×10^{-9} ergs s^{-1} cm^{-2}, and the luminosity 2850 $L_\odot$. The relatively low luminosity of I19024, in comparison with stellar evolutionary models, indicates that the initial mass of its central star was ~1–1.5 $M_\odot$. The lobes, which appear to be hollow structures with dense walls, have a total mass greater than or equal to about 0.02 $M_\odot$. The dusty tori in the center have masses of a few times 10^{-3} $M_\odot$. The faint halo has a power-law radial surface brightness profile with an exponent of about -3 and most likely represents the remnant spherical circumstellar envelope formed as a result of constant mass loss during the AGB phase over the past several thousand years. From the CO data we infer a molecular mass $\gtrsim0.025$ $M_\odot$ and an expansion age $\lesssim2870$ yr, giving a mass-loss rate $\gtrsim10^{-5}$ $M_\odot$ yr^{-1}. The far-infrared fluxes of I19024 indicate the presence of a large mass of cool dust in the nebula; from a simple model we infer the presence of "cool" (109 K) and "warm" (280 K) components of dust mass 5.7×10^{-4} and 1.5×10^{-7} $M_\odot$. We discuss our results for I19024 in the light of past and current ideas for the dramatic transformation of the morphology and kinematics of mass-ejecta as AGB stars evolve into planetary nebulae.

Subject headings: circumstellar matter — ISM: refection nebulae — planetary nebulae: general — stars: AGB and post-AGB — stars: individual (IRAS 19024+0044) — stars: mass loss

Online material: color figures

1. INTRODUCTION

Preplanetary nebulae (PPNs), short-lived transition objects between the asymptotic giant branch (AGB) and planetary nebula (PN) phases, probably hold the key to understanding how the slowly expanding (5–15 km s^{-1}), largely spherical, circumstellar envelopes (CSEs) of AGB stars (e.g., Neri et al. 1998) transform

into highly aspherical PNs with fast outflows ($\gtrsim100$ km s^{-1}) along one or more axes (e.g., Balick & Frank 2002; Sahai & Trauger 1998). *Hubble Space Telescope* (*HST*) imaging of PPNs has shown the widespread presence of diverse aspherical morphologies (e.g., Ueta et al. 2000; Kwok et al. 2000; Hrivnak et al. 1999; Sahai et al. 1998a, 1998b, 1999a, 1999b, 1999c; Sahai 1999). In addition to the morphological data, high angular resolution kinematical data are sorely needed to construct and test theoretical models. However, such kinematical data are available for very few PPNs—first, these objects are generally compact (size $\lesssim5''$), and second, since the bulk of the nebular material in these objects is largely neutral, there is a general lack of nebular optical emission lines in their spectra.

We are therefore carrying out a program of multiwavelength imaging and spectroscopic observations of young PPNs, using a large (~300), morphologically unbiased sample (Sahai & Sánchez Contreras 2004) constructed from catalogs of OH/IR stars (evolved, visually faint, mass-losing stars with dense circumstellar envelopes, showing generally double-peaked OH maser emission). Interferometric maps of the OH emission in many of these objects (e.g., Bowers et al. 1983) shows that it typically arises in an extended circular shell of radius $\sim10^{16}$ cm,

---

[1] The phrase "preplanetary nebula," which refers to an object in the evolutionary phase immediately preceding the planetary nebula phase, is used in this paper in place of the more commonly used "proto–planetary nebula," because the term "proto–planetary" is widely used to refer to disks around pre–main-sequence stars. Since the term protoplanet is used by the planet and planet formation communities to refer to planets undergoing formation, the use of the term "protoplanetary nebula" to refer to a completely different kind of object is an unfortunate choice, which compounds our inconvenience of having the historically inherited misnomer "planetary nebula." We believe, therefore, that it is important to replace the term "proto–planetary nebula" (in this work and future studies) with "preplanetary nebula," which is both unique (in the planetary community, the term "preplanet" is not used, and never will be) and correct in its meaning.

[2] Jet Propulsion Laboratory, MS 183-900, Caltech, Pasadena, CA 91109; raghvendra.sahai@jpl.nasa.gov.

[3] Astronomy Department, Caltech, MS 105-24, Pasadena, CA 91125.

[4] Division of Astronomy and Astrophysics, UCLA, Los Angeles, CA 90095.

indicating that substantial AGB mass-loss has occurred through a spherical outflow. The *IRAS* spectral energy distributions (SEDs) of a large fraction of these objects indicate a lack of hot ($\sim$1000 K) dust (12-to-25 μm flux ratio $F_{12}/F_{25} < 1$), implying a recent decrease in their mass-loss rates, marking the beginning of their post-AGB evolution.

Two *HST* SNAPshot imaging surveys of our young PPN sample are underway, and a third one has been completed— a substantial number of objects have been resolved and show bipolar or multipolar morphologies (e.g., Sahai 2004). Detailed studies of the best-resolved objects are now in progress— we recently reported the discovery of an icy, bipolar young PPN with knotty jets from one of these surveys (Sahai et al. 2003). We now present our optical and infrared *HST* imaging of IRAS 19024+0044 (hereafter I19024; also OH 035.209−02.653 [Sevenster et al. 2001]), together with ground-based optical spectroscopy and interferometric millimeter-wave mapping observations. These data, together with archival infrared and far-infrared data from *IRAS* and *Midcourse Space Experiment* (*MSX*), have been analyzed to determine the physical characteristics of this young PPN. We have found that I19024 shows multiple, diametrically opposed lobes that provide extremely important clues to the process or processes that shape planetary nebulae. Detailed studies of clear examples of the multipolar morphology, such as I19024, provide us with the best opportunity to constrain these processes.

The rest of the paper is organized as follows: § 2 describes our multiwavelength imaging and spectroscopic observations; § 3 describes the results of these observations; an estimate of the distance to this object is presented in § 4; a discussion of the optical spectrum and its implications for the spectral type of the central star and the presence of fast outflows is presented in §§ 5 and 6; the *HST* images are analyzed in §§ 7–9 to derive the physical characteristics of individual nebular structures; the molecular and dust masses are estimated in § 10 by modeling far-infrared and millimeter-wave data; the structure and formation of I19024 is discussed in the context of theoretical models in § 11; and finally, our main conclusions are summarized in § 12.

2. OBSERVATIONS

2.1. *Optical and Near-Infrared Imaging with HST*

I19024 was imaged on UT date 2003 March 18 (GO program 9463), by the High Resolution Camera (HRC) of the Advanced Camera for Surveys (ACS), which has a plate scale of 0″025 pixel^{-1}, using the F606W filter ($\lambda = 0.60$ μm, $\Delta\lambda = 0.123$ μm; exposures were 2×400 s) and the F814W filter ($\lambda = 0.80$ μm, $\Delta\lambda = 0.149$ μm; exposures were 2×70 s). We also obtained images with Camera 1 of the Near Infrared Camera and Multi-Object Spectrometer (NICMOS) on UT date 2003 September 7 (GO program 9801) using the F110W ($\lambda = 1.1$ μm, $\Delta\lambda = 0.55$ μm; total exposure time was 479.95 s) and F160W ($\lambda = 1.6$ μm, $\Delta\lambda = 0.4$ μm; total exposure time was 207.89 s) filters (GO program 9801). All images were obtained with a two-point dither, and the standard STScI/*HST* pipeline calibration has been applied to all data. For ease of comparison, the NICMOS images have been rotated to the same orientation as the HRC/ACS images. We have preserved the intrinsic orientation of the HRC images in the figures in this paper, electing not to rotate them for alignment of their horizontal and vertical axes with the cardinal directions, because such rotation would result in some degradation of the image quality. Numerous field stars present in the images have been used to achieve

satisfactory registration between the optical and near-infrared images.

2.2. *Long-Slit Optical Spectroscopy*

A long-slit, low-resolution ($\Delta\lambda = 9.8$ Å) optical spectrum was obtained on 2002 June 30 using the facility spectrograph on the 1.5 m Palomar Telescope and a 2″-wide slit oriented at a position angle (P.A.) of 90°; seeing was $\sim$2″1.[5] Echelle spectra were obtained with the 10 m Keck II telescope (Mauna Kea, Hawaii) on 2003 June 1 using the Echelle Spectrograph and Imager (ESI).[6] The detector was a MIT-LL CCD with 2048×4096 pixels of 15 μm. Total wavelength coverage is $\sim$3900–11000 Å. The reciprocal dispersion and the pixel angular scale range from 0.15 to 0.39 Å pixel^{-1} and from 0″120 to 0″168, respectively, for 10 echellette orders. We used a 0″5$\times$20″ slit oriented at P.A. $= -42°$. Total integration time was 2400 s. Data were reduced using IRAF.[7] We used CuAr lamps to perform wavelength calibration. The velocity resolution achieved (FWHM of the lamp lines) is $\sim$37 km s^{-1} for all orders. Two photometric standards, LTT 9239 and Feige 110 were used for flux calibration. Seeing was $\sim$0″6. Weather conditions were non-photometric during both the Keck and Palomar observations.

2.3. *Millimeter-Wave Interferometric Observations*

Interferometric mapping of the CO $J = 1-0$ emission line (with rest frequency 115.271204 GHz) in I19024 was carried out using the millimeter interferometer of the Owens Valley Radio Observatory (OVRO), which consists of six 10.4 m diameter antennas.[8] Observations were performed on 2002 October 23 in low (L) configuration, for which baselines between antennas range from 15 to 115 m. The units of the digital spectral line correlator were arranged to provide a total bandwidth of 90 MHz ($\sim$234 km s^{-1}) with a channel spacing of 1 MHz (2.6 km s^{-1}). The 3 mm continuum emission from I19024 was observed simultaneously using the dual-channel analog continuum correlator, which provided a total bandwidth of 4 GHz (after combining both IF bands). Total duration of the track (including integration time on source and calibrators) was $\sim$4 hr.

The calibration of the data was performed using the MMA sofware package.[9] Data were gain-calibrated in baseline-based mode using the quasar J1751+096, which was observed at regular time intervals of $\sim$20 minutes before and after each target observation. The quasar 3C 454.3 was used as passband and flux calibrator.

Reconstruction of the maps from the visibilities was done using the Multichannel Image Reconstruction, Image Analysis and Display (MIRIAD) software. We Fourier transformed the measured visibilities with robust weighting, which is an optimized compromise between natural and uniform weighting. After that, data were cleaned and maps restored. The clean beam for our CO maps has FWHM $= 5″84\times3″41$ and is oriented at P.A. $= -16°$. The noise (1 σ) in the CO and continuum maps
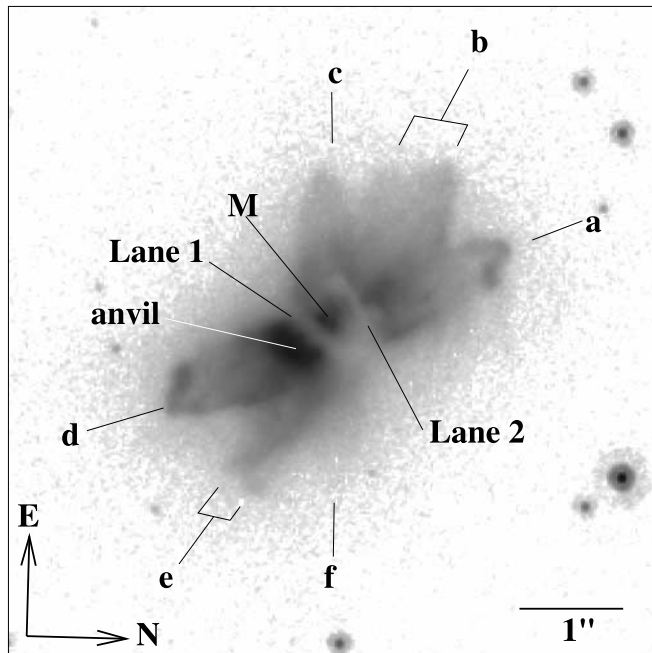
FIG. 1.—Image (*log stretch*) of the preplanetary nebula IRAS 19024+0044, made using exposures taken with *HST*/ACS through the F606W filter. The maximum (*black*) and minimum (*white*) intensities of the gray scale are 4.68×10^{-3} and 3.71×10^{-6} mJy arcsec^{-2}, respectively. Lobes b and e may be composite.
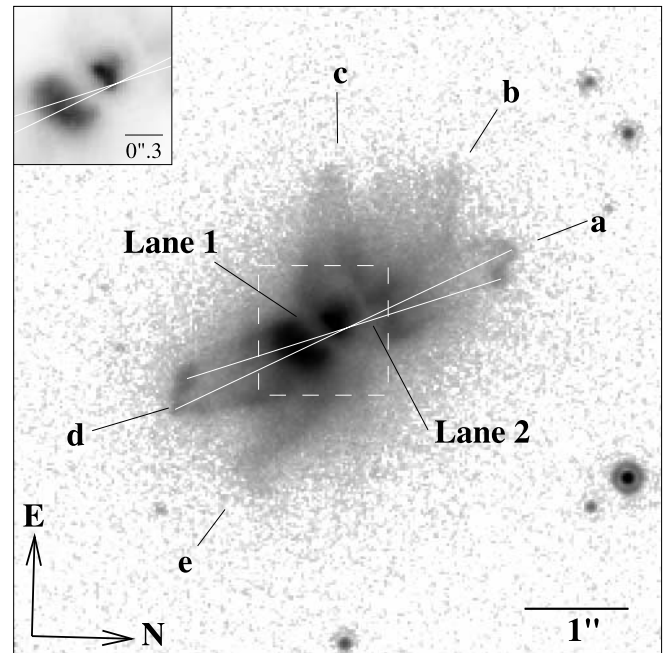

FIG. 2.—Image (*log stretch*) of the preplanetary nebula IRAS 19024+0044, made using exposures taken with *HST*/ACS through the F814W filter. The maximum (*black*) and minimum (*white*) intensities of the gray scale are 7.33×10^{-3} and 2.32×10^{-5} mJy arcsec^{-2}, respectively. Inset is an expanded view of the central region (*square with dashed sides*) on a linear scale. Two straight lines join diametrically opposed regions in the point-symmetric tips of lobe pair *a-d*.

is ∼80 and 2 mJy beam^{-1}, respectively. The conversion factor from surface brightness to temperature units is 4.63 K/(Jy beam^{-1}).

3. RESULTS

3.1. *Optical and Near-Infrared Imaging*

Both the F606W and F814W images (Figs. 1 and 2) show a multipolar nebula of size ∼3″.7×2″.3. At least six (a–f) elongated lobes can be seen emanating from the center of the nebula. In the F606W image, where the lobes are seen with higher contrast against the background, both b and e appear to have two components each, and each may thus be a superposition of two lobes due to close proximity and/or projection effects. Lobes a and d show limb-brightened, structured tips, the structure of which appears to be point-symmetric about a central location in the nebula. The lobe pairs a-d, b-e, and c-f are oriented along P.A.s of 25°, 55°, and 92°, respectively. The central region shows two dark lanes ("lane 1" and "lane 2") southwest and northeast of a central, shallow, maximum (M), respectively. Lane 1 is bounded on its southwest side by a bright region ("anvil"). A very faint, presumably surface brightness–limited, diffuse halo surrounds the lobes.

The NICMOS F110W and F160W images show the same major lobe structures as seen in the optical images (Figs. 3 and 4). A color composite, made from the F606W, F110W, and F160W images, is shown in Figure 5. The central region (lanes 1, 2, and feature M) is significantly redder than the lobes and shows marked brightness differences as a function of wavelength (Fig. 6). Feature M gets progressively brighter, and the anvil fainter, with increasing wavelength; at the longest wavelength, M is the brightest region of the nebula. The location of peak intensity within M also shifts steadily with wavelength. This peak has its most compact appearance in the F160W image—we have labeled its location in this image (Fig. 4) as "P." P is much redder than the lobes, and it lies on or very

close to the center of symmetry of the point-symmetric tips of the a-d lobe pair (denoted by the intersection of two white lines joining diametrically opposed regions in the tips in Figs. 2–4).

The lobes are seen predominantly in light from the central star, scattered by dust in the lobes. Limb-brightening effects can be seen for several lobes, suggesting that they are dense-walled
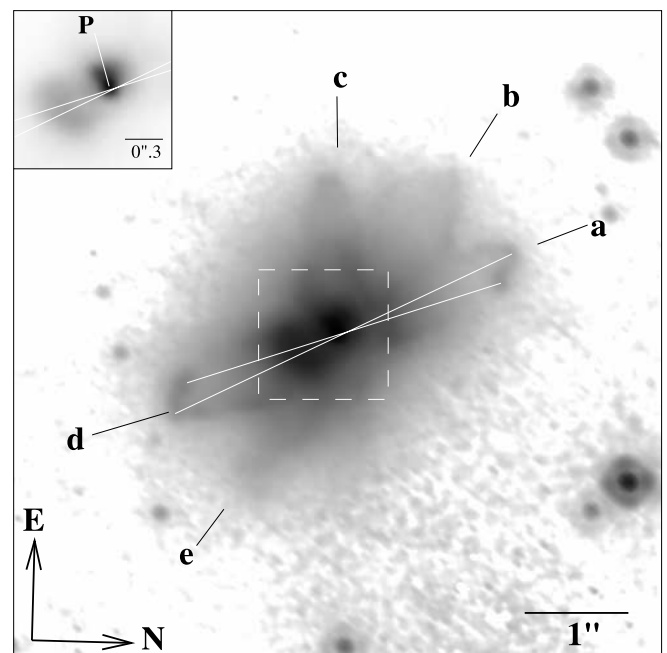

FIG. 3.—As in Fig. 2 (*image and inset*), but taken with the F110W filter using *HST*/NICMOS. The maximum (*black*) and minimum (*white*) intensities of the gray scale are 6.07×10^{-3} and 2.42×10^{-6} mJy arcsec^{-2}, respectively.
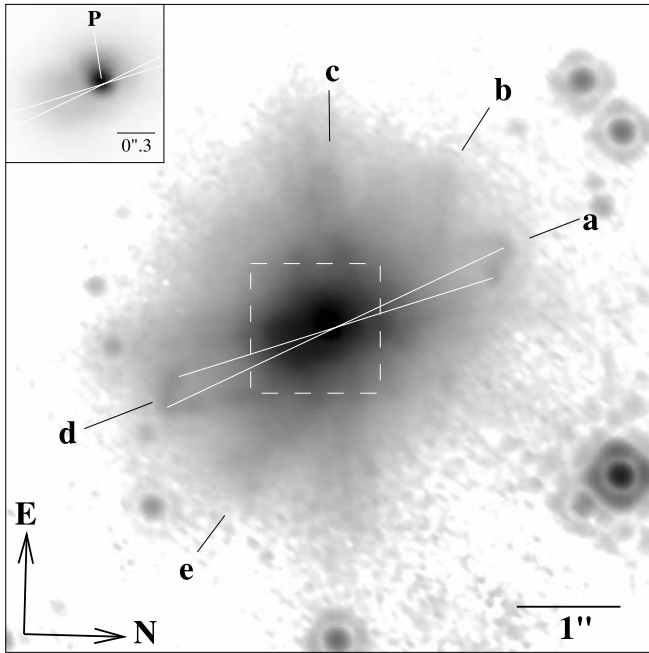
FIG. 4.—As in Fig. 2 (*image and inset*), but taken with the F160W filter using *HST*/NICMOS. The maximum (*black*) and minimum (*white*) intensities of the gray scale are 5.14×10^{-3} and 2.58×10^{-6} mJy arcsec^{-2}, respectively.

FIG. 6.—Color image (*linear stretch*) of the central region of I19024, made by combining the F606W (*blue*), F110W (*green*), and F160W (*red*). The orientation of this image is identical to that in Figs. 1–4.

structures with tenuous interiors. The color of the lobes does not change strongly along their length beyond the central region, which supports the idea that these are relatively hollow so that the starlight does not experience an increasing amount of reddening while traversing the lobes, before being scattered by dust in the lobe walls. Lanes 1 and 2 are much more difficult to see in the NICMOS images, becoming virtually indistinguishable from the surrounding nebulosity in the F160W image, presumably as a result of their lower optical depths at the longer wavelengths.
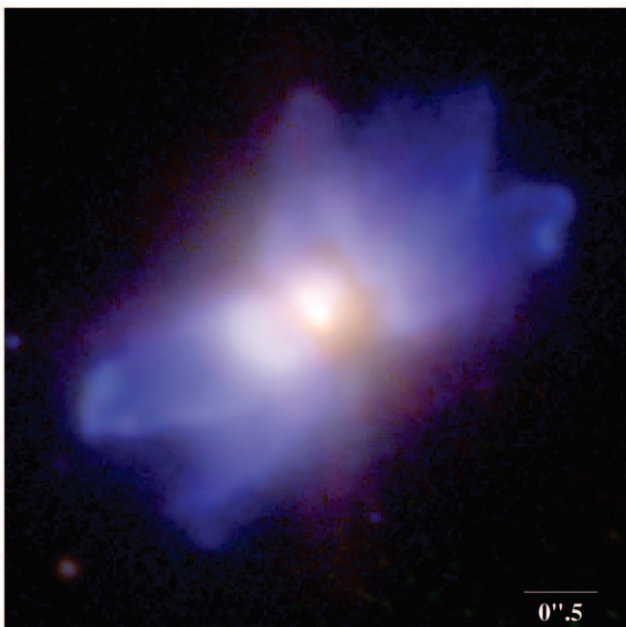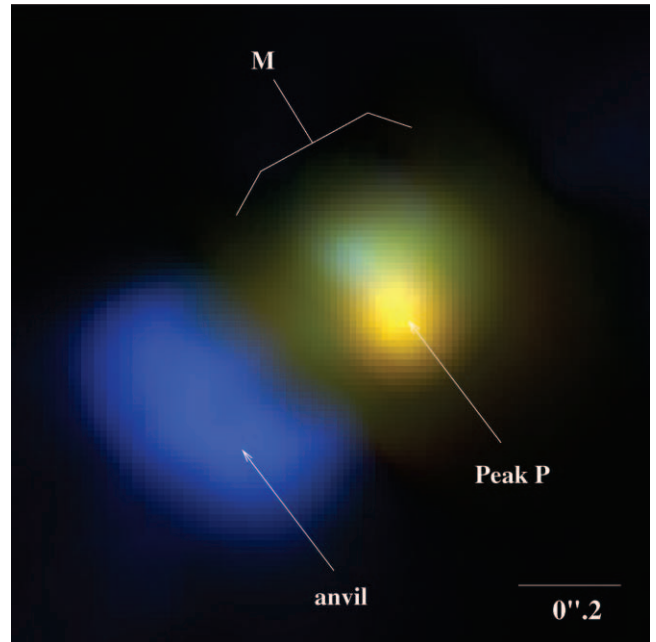

FIG. 5.—Color image (*log stretch*) of I19024, made by combining the F606W (*blue*), F110W (*green*), and F160W (*red*) images. The orientation of this image is identical to that in Figs. 1–4.

Using the photometric calibration keywords in the image headers, we find that the integrated fluxes for the nebula at 0.6, 0.8, 1.1, and 1.6 μm are 1.2, 4.7, 17.3, and 30.3 mJy, corresponding to magnitudes[10] of $R = 15.7$, $I = 14.1$, $J = 12.5$, and $H = 11.3$. Our measured magnitudes are in reasonable agreement with those from the Two Micron All Sky Survey[11] ($J = 12.4 \pm 0.2$ and $H = 11.5 \pm 0.2$) and USNO-B.1[12] ($R = 15.1$ and 15.4, and $I = 14.4$) catalogs. The USNO-B.1 gives B magnitudes of 18.75 (16.98) for epoch 1(2) for I19024; however, the decrease in B magnitude is most likely not real;[13] we think it is due to systematic calibration uncertainties because other field stars around I19024 show very similar changes in their cataloged blue magnitudes. Using the USNO-B.1 coordinates for three field stars in the ACS images, we find that peak P is located at $\alpha = 19^{\mathrm{h}}05^{\mathrm{m}}02\overset{s}{.}06$, $\delta = 00°48'51\overset{''}{.}3$ (J2000.0).

3.2. Optical Spectroscopy

Both the Palomar 1.5 m and Keck data show a spatially compact source of Hα emission. Since the orientation of the ESI slit was set to be along the parallactic angle, which corresponded to P.A. $= -42°$, the unfortunate result was that the extended lobe regions were not sampled by the ESI slit. Hence potential sources of shocked gas emission in the lobes, such as the bright tips of the lobe pair a-d, were not probed by the ESI spectra. The Hα line in the ESI spectrum shows a strong, narrow

---

[10] In order to convert from the fluxes measured in the different filters above to magnitudes, we have used the Units Conversion Tool at http://www.stsci.edu/hst/nicmos/conversion_form.html, assuming a $T_{\mathrm{eff}} = 5200$ K stellar blackbody to describe the spectral energy distribution (see § 5.1); the results are not very sensitive to the adopted T_{eff}.

[11] Source name in catalog: J19050205+0048508; J2000.0 coordinates: $\alpha = 19^{\mathrm{h}}05^{\mathrm{m}}02\overset{s}{.}06$, $\delta = 00°48'50\overset{''}{.}9$.

[12] Source name in catalog: B1.0 0908-0386880; J2000.0 coordinates: $\alpha = 19^{\mathrm{h}}05^{\mathrm{m}}02\overset{s}{.}06$, $\delta = 00°48'51\overset{''}{.}1$.

[13] Such a decrease has been observed in the PPN CRL 618 and attributed to a temporal decrease in the dust extinction (Gottlieb & Liller 1976; Sánchez Contreras et al. 2002).
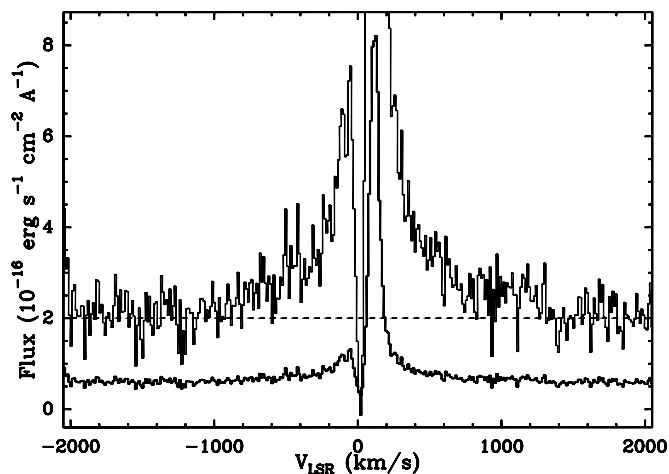
FIG. 7.—Hα emission from IRAS 19024+0044, obtained with Keck II ESI: the top curve shows the calibrated spectrum scaled and shifted vertically by arbitrary factors (but on the same velocity scale) in order to show the weak wings more clearly. [*See the electronic edition of the Journal for a color version of this figure.*]

($\Delta V_{\rm FWHM} = 78$ km s^{-1}) central core peaking at $V_{\rm lsr} = 102$ km s^{-1}. It also has a narrower ($\Delta V_{\rm FWHM} = 60$ km s^{-1}) blueshifted absorption feature, located at $V_{\rm lsr} \sim -3$ km s^{-1} (Fig. 7), and broad weak wings extending to more than ± 1000 km s^{-1} at zero intensity. The Hα line core is asymmetric with a blue wing that slopes much more steeply than the red wing. Weaker Hβ emission can be clearly seen in the ESI spectrum (emission peak at $V_{\rm lsr} = 99$ km s^{-1}, absorption peak at $V_{\rm lsr} \sim 12$ km s^{-1}), which has a higher signal-to-noise ratio (S/N) than the Palomar one. Many Fe II lines having P Cygni profiles can be seen in the

high S/N regions of the ESI spectrum that are relatively free of telluric contamination—the most prominent of these have rest wavelengths of 5018.44, 5169.03, 5234.63, 5316.23, and 6247.19 Å. The Fe II emission features are centered ∼55 km s^{-1} redward of the systemic velocity ($V_{\rm lsr} = 50$ km s^{-1}; see § 3.3), and the absorption features are blueshifted from the emission peaks by about 70–80 km s^{-1}.

The full spectrum shows a relatively featureless and fairly red continuum and lacks the strong forbidden emission lines characteristic of PNs (Fig. 8). It is thus clear that I19024 has not yet reached the planetary nebula phase.

3.3. *Millimeter-Wave Observations*

Our interferometric mapping of CO $J = 1-0$ emission toward I19024 is shown in Figure 9. A map of the emission, summed over the central three channels in order to increase the S/N, is also shown. The source appears to be marginally resolved along the minor axis of the elliptical beam; an elliptical Gaussian fit to this map gives a major (minor) axis of size (FWHM) $5\farcs5 \pm 0\farcs1$ ($4\farcs4 \pm 0\farcs1$); the major axis is oriented at a P.A. of 29°, which is roughly along the a-d lobe axis. The peak emission in this map is located at $\alpha = 19^{\rm h}05^{\rm m}02\fs02$, $\delta = 00°48'51\farcs2$ (J2000.0). The integrated $J = 1-0$ line profile (Fig. 10) is quite broad (typical of CO profiles from the circumstellar envelopes of AGB stars) and is centered at $V_{\rm lsr} = 50$ km s^{-1}. The full-width at zero intensity is about 26 km s^{-1}, implying an expansion velocity of the molecular envelope of $V_{e,\rm AGB} \sim 13$ km s^{-1}, which is a typical value for the circumstellar envelopes of AGB stars. Both the systemic and expansion velocity derived from the CO line agree well with the corresponding values ($V_{\rm lsr} = 50$ km s^{-1} and $V_{e,\rm AGB} = 13.6$ km s^{-1}) derived using the velocities of the red and blue peaks of
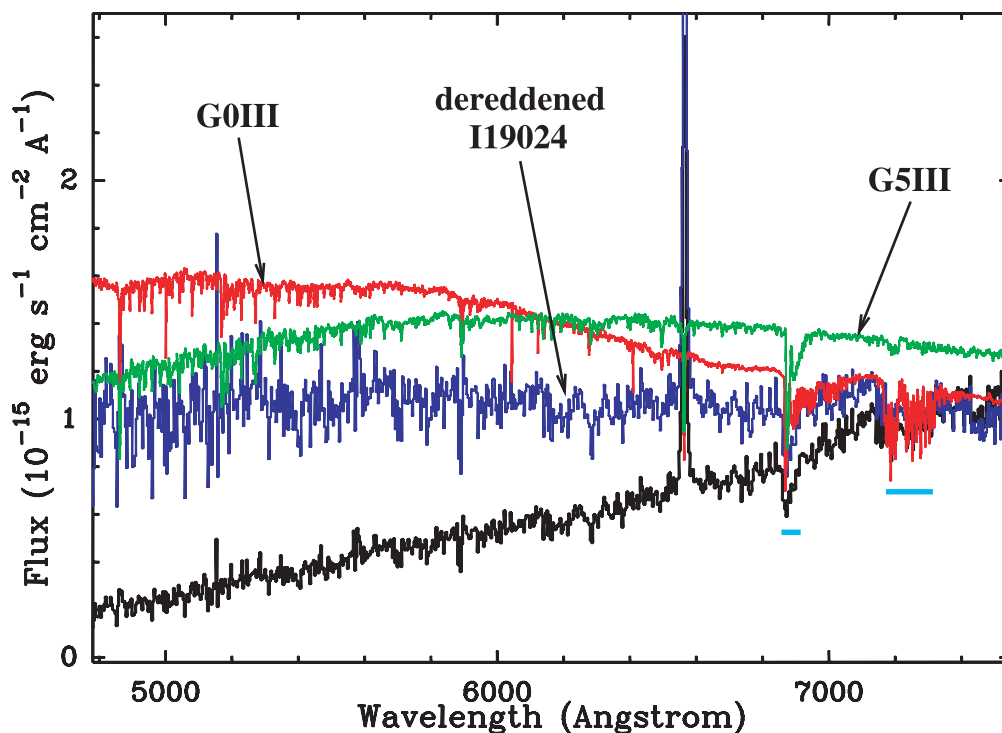

FIG. 8.—Intrinsic (*black*) and de-reddened (*blue*) low-resolution optical spectra of IRAS 19024+0044 obtained with the Palomar 1.5 m facility spectrograph, shown with G0 (*red*) and G5 (*green*) giant spectra for comparison. Horizontal cyan bars indicate regions affected by telluric features.
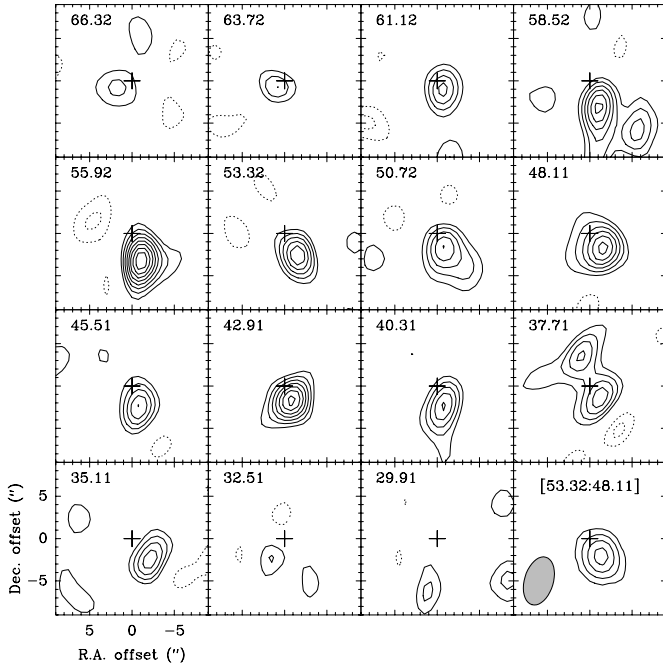
FIG. 9.—CO $J = 1-0$ channel maps of IRAS 19024+0044, obtained at OVRO. The numbers in the top left hand corner of each panel gives the channel velocity (V_{lsr}). Contour levels are $-2, 2, 3, \ldots, \sigma$ (spaced every $1 \sigma = 83$ mJy beam^{-1}) for all panels except the one at bottom right corner—in this panel, the emission has been summed over the three channels centered on the systemic velocity (panels with channel velocity 53.32, 50.72, and 48.11 km s^{-1}) in order to increase the S/N, and contour levels are 30% to 90% in steps of 20% of the peak intensity. The map reference center in each panel, indicated by a cross, is located at $\alpha = 19^h05^m02^s.11$, $\delta = 00°48'53''.28$ (J2000.0) (slightly offset from the center of the nebula).
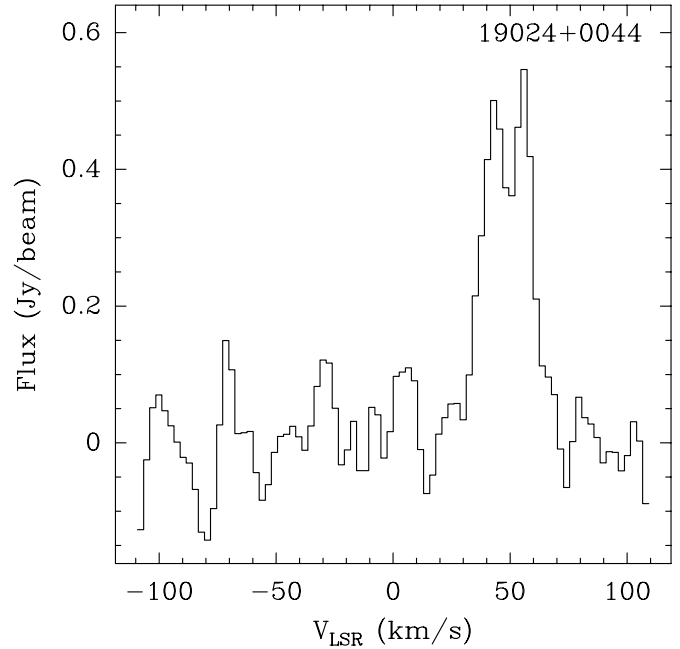

FIG. 10.—CO $J = 1-0$ spectrum of IRAS 19024+0044, obtained at OVRO. The conversion factor from surface brightness to temperature units is 4.63 K/(Jy beam^{-1}).

the OH maser profile (Sevenster et al. 2001). No continuum emission was detected, with a 3σ upper limit of 6 mJy.

4. DISTANCE AND LUMINOSITY

We use the systemic radial velocity, $V_{lsr} = 50$ km s^{-1}, and a simple Galactic rotation model, to determine the "kinematic" distance to I19024.

For a simple rotation law, $v_r = AD \sin 2l \cos^2 b$ (Goodrich 1991), where v_r is the radial velocity, $A = 14.4 \pm 1.2$ km s^{-1} kpc^{-1}, D is the distance in kpc, and (l, b) are Galactic coordinates. For I19024, $v_r = 50$ km s^{-1}, and $(l, b) = (35°.21, -2°.65)$, hence $D = 3.5$ kpc. We assume this value of the distance for the rest of the paper and provide the dependence of important physical properties on it as necessary. From a model fit to the observed spectral energy distribution (§ 10), we derive a bolometric flux of 7.3×10^{-9} ergs s^{-1} cm^{-2} and a luminosity of $2850 (D/3.5)^2 L_\odot$.

In the following sections we have corrected our measured intensities from the *HST* images for interstellar extinction using $A_V = 1.4$, derived using the numerical algorithm provided by Hakkila et al. (1997), which computes the three-dimensional visual interstellar extinction and its error from inputs of Galactic longitude and latitude, and distance, from a synthesis of several published studies. This estimate is consistent with the Galactic extinction map provided by Whittet (1992, p. 67).

5. THE CENTRAL STAR

5.1. *Spectral Type*

It is not easy to estimate a spectral type for the central star of I19024 because of the presence of strong emission in

the Balmer lines (and thus the possibility that such emission also contaminates other diagnostic stellar absorption lines), together with the limited S/N ratio of the spectrum in wavelength regions where various diagnostic lines for spectral typing are found. The difficulty of assigning spectral types is a common problem for post-AGB stars since a significant fraction of these show Balmer emission lines with P Cygni shapes; the emission is often variable (e.g., Roberts 22; Allen et al. 1980). The I19024 spectrum clearly does not show the very strong Paschen absorption profiles seen in early-type stars (which have equivalent widths EW $\sim 6-7$ Å); weak candidate features (with EW $\sim 0.3-0.6$) are seen near the rest wavelengths of the P 9– 18 lines (9229–8438 Å). However, because of the relatively large number of absorption features in this wavelength region with comparable equivalent widths, we cannot be totally sure of the identification of our Paschen series candidates. Furthermore, since Paschen lines, like the Balmer lines, can also be in emission (e.g., Hen 3−1475; Riera et al. 1995), they are not a good diagnostic of the spectral type in I19024. Finally, the average V_{lsr} of our Paschen series candidates is about 40 ± 10 km s^{-1}, close to or slightly blueshifted from the systemic velocity.

The relatively featureless, red spectrum seen in I19024 is seen commonly toward other PPNs, and the lack of metallic absorption lines has previously been interpreted as resulting from the star being of an early spectral type (e.g., A0 in Roberts 22; Allen et al. 1980; B in He 3−1475, Riera et al. 1995). However, since metallic lines can occur in emission in many post-AGB stars, such emission can fill in stellar absorption features, thus masking their intrinsic absorption equivalent widths. For example, in the red part of the spectrum, the Ca II triplet at 8498, 8542, and 8662 Å, is quite strong in G and F spectral types (e.g., total EWs of $\sim 3-6$ Å) and starts weakening significantly in early A-type objects; however, this triplet can occur in emission in PPNs, as, e.g., in He 3−1475 (Riera et al. 1995), so it cannot be used as a reliable diagnostic for I19024.

At shorter wavelengths, the presence (absence) of the G band due to CH at 4300 Å (covering a range of about 30–40 Å) and the Mg I triplet (5167, 5173, and 5184 Å) has traditionally been used as indicative of later (earlier) spectral types. However, our upper limit for I19024 (EW $\lesssim$ 6 Å) for the G band is too insensitive to discriminate against spectral types even as late as G5 (where EW $\sim$ 5–6 Å; the G band increases in strength toward later spectral types). The Mg I $\lambda\lambda$5173, 5184 lines are not seen, with EW $\lesssim$ 0.15 Å for each (the λ5168 line region contains an Fe II P Cygni line), which would suggest a spectral type F0 or earlier, in the absence of any filling-in due to emission. Although the Na I D lines are seen in absorption, these are anomalously strong, considering the absence of the Mg I lines, and are centered at $V_{lsr} = 38$ km s^{-1}, blueward of the systemic velocity. The Na I D lines are thus most likely of interstellar origin.

Two prominent absorption features, due to the O I triplet at 7771.9, 7774.2, and 7775.4 Å, are seen in our spectrum, with EWs of 0.8 Å (7771.9 Å) and 1.1 Å (7774.2+7775.4 Å). The O I triplet is well known as a luminosity indicator, and the large EWs we observe are restricted to Class I sources—specifically the combined EW we measure (1.8 Å) is only found for Class Ia sources of spectral type between G0 and F8 (Thomas et al. 1979). These features are centered at $V_{lsr} \sim 45$ km s^{-1} (roughly similar to the average V_{lsr} of the candidate Paschen lines) and close to the systemic velocity ($V_{lsr} = 50$ km s^{-1}).[14] Additional absorption features are seen in the vicinity of the Si II lines at 6347.11 and 6371.37 Å, centered at $V_{lsr} = 45$ km s^{-1}, and the K I lines at 7664.91 and 7698.97 Å, centered at $V_{lsr} = 26$ km s^{-1}. An emission feature, seen at 6318.6 Å, if identified as the Mg I triplet (6318.72, 6319.24, and 6319.50 Å), is centered at $V_{lsr} = 9$ km s^{-1}. The large spread in the radial velocities of the O I, Si II, and K I absorption features is somewhat puzzling; one explanation is that they arise in different regions of a kinematically complex outflow.

We have corrected the Palomar and Keck spectra of I19024 for reddening (due to both circumstellar and interstellar dust) using an average extinction, $A_V = 3.6$, derived from the Hα-to-Hβ emission-line ratio. The resulting Keck dereddened spectrum of I19024 shows a relatively shallow slope over a very wide range of wavelengths—the 4700-to-8500 Å flux ratio, $F_{47/85} = 1.64$, compared to 1.9–5.9 for G0–F2 spectral types. Thus, based on the continuum slope, I19024's central star is later than G0, and since for a G5 star (1) the SED has a maximum between 4700 and 8500 Å and (2) $F_{47/85} = 0.98$, it is likely that I19024's central star is earlier than G5.

In summary, the central star of I19024 has evolved off the AGB and is now presumably moving on a horizontal track leftward in the H-R diagram at a constant luminosity. Comparing our estimated value of the latter, 2850 $L_\odot$, with the evolutionary models by Vassiliadis & Wood (1994), we find that only models with the smallest main-sequence masses (1 $M_\odot$) have luminosities on the horizontal post-AGB track that are close to that of I19024, e.g., a 1 (0.95) $M_\odot$ star that left the AGB during the H (He) burning shell phase of its thermal pulse cycle has a luminosity of 3470 (3160) $L_\odot$ on the horizontal track. However, our value of I19024's luminosity can easily have been underestimated by a factor of 2 because of the uncertainty in the distance, allowing models with main-sequence masses of up to $\sim$1.5 $M_\odot$ to be considered acceptable.

5.2. *Is Peak P the Central Star?*

Is this peak, which is quite compact and bright in the F160W image, the attenuated central star? First, the peak has a non-stellar appearance. Second, we use a quantitative argument, described by Sahai et al. (2003), to investigate the nature of the central peak in the PPN IRAS 22036+5306, to settle this issue. If P consists of direct but attenuated light from the central star, then the line-of-sight extinction to the latter can be estimated by comparing the observed ratio of the 1.1 and 1.6 μm fluxes ($R_{1.1/1.6}$) in P to its unattenuated value estimated from the bolometric flux and temperature of the central star ($T_{eff} = 5200$ K, based on a spectral type between G0 and G5[15]). We find that the observed value for $R_{1.1/1.6}$ (corrected for interstellar extinction) is $\sim$0.5, whereas the expected value is 1.25, implying a small line-of-sight extinction, $\tau_{1.6\,\mu m} = 0.87$. We have used standard small-grain (size $\sim$0.1 μm) dust properties from Whitney (1995), in which the decrease in extinction opacity from 1.6 to 1.1 μm can be described as a power law, λ^{-q}, where $q = 1.9$. If, however, the dust grains are larger, as indicated by our analysis of dust in lanes 1 and 2 and in the lobes (§§ 7 and 8), the value of q will be lower. If we assume $q = 1$, then the line-of-sight extinction, $\tau_{1.6\,\mu m} = 2.0$. In contrast, the absolute 1.6 μm flux of P (given its bolometric flux; § 4) implies a much larger value of $\tau_{1.6\,\mu m} \sim 5.6$. Peak P is therefore not the central star, but most likely results from starlight scattered by the innermost regions of a dense dusty region surrounding the latter, and is therefore expected to be located close to it. This expectation is supported by the location of P at or very close to the center of symmetry of the lobe pair a-d, assuming that the lobes result by outflow of matter and energy from (or very near) the central star.

6. POST-AGB OUTFLOWS

The peculiar Hα line shape in I19024 (i.e., with a narrow, intense emission core and broad, weak wings, and blueshifted absorption), seen in many PPNs (van de Steene et al. 2000; Sahai & Sánchez Contreras 2004; Sánchez Contreras et al. 2003), is most simply interpreted in terms of the following model— the broad emission profile arises from a compact central source;[16] this emission (and stellar continuum) is scattered by dust in the walls of the nebular lobes, and the blueshifted absorption is due to neutral or partially ionized outflowing gas in the lobes absorbing the scattered photons. Such a model has been successful in producing a detailed fit to the spatiokinematic distribution of the blueshifted absorption in the Hα line profiles observed with *HST*/STIS in the PPN Hen 3−1475 (Sánchez Contreras & Sahai 2001). The scattering should produce an overall redshift of the emission line profile relative to the systemic radial velocity, and this is what we observe in I19024— the Hα emission peak is located 52 km s^{-1} redward of the systemic velocity of I19024, as measured from CO and OH data.

What is the nature of the outflow that produces the absorption in the Balmer lines? As in the case of Hen 3−1475, we argue that it is most likely a "pristine" post-AGB wind from (or near)

---

[14] Using the known wavelengths of numerous atmospheric emission features, as well as the O_2 A-band absorption features, we have checked that our wavelength calibration is correct to better than 0.1 Å.

[15] Although the spectral type of the star is quite uncertain and may be earlier than G0, our results in this and the following sections do not change qualitatively for higher values of T_{eff}.

[16] No profound explanation has yet been proposed for these very broad wings in the Hα line, which have been also been found in young, compact PNs, although possible mechanisms include emission from a very high velocity outflow, Raman scattering, and/or Keplerian rotation in a dense disk; a more detailed discussion of the origin of these wings is deferred to another paper.

the central star. The label "post-AGB" is used in order to discriminate between the fast wind[17] and the slow progenitor AGB wind and is not meant to imply that the former originates directly from the post-AGB central star. In fact, a favored model for the fast outflow requires it to be powered by an accretion disk around a companion star, with the accretion disk resulting from gravitational capture of a fraction of the mass lost by the AGB progenitor star (Morris 1987, 1990). The speed of the bulk of the material in the fast outflow is $V_f \sim 100$ km s^{-1}, derived from the blue-shift of the absorption feature relative to the emission feature in the Hα line; however, the absorption feature is quite broad, indicating the presence of smaller amounts of material expanding as fast as ~ 150 km s^{-1}. It is plausible that the outflow is kinematically complex, with the outflow speed having a radial or latitudinal dependence. The smaller outflow speed derived from the Fe II P Cygni lines (~ 70 km s^{-1}) support this idea.

Such an outflow is seen in the PPN IRAS 16342−3814, where OH masers trace a slower, low-latitude component, and H$_2$O masers trace the fastest moving material along the polar axis (Morris et al. 2003).

7. DUST LANES 1 AND 2

The true three-dimensional structures of the features labeled "lane 1" and "lane 2" are unknown. One plausible hypothesis (the "two-tori" hypothesis) is that they are two independent toroidal structures. The inference of a toroidal shape for lane 1 is based on the fact that it appears to form the commonly occurring dense central waist of a bipolar PPN, seen roughly edge-on, and that such waists are widely believed to represent dusty toroidal structures in bipolar PPNs, and for lane 2 is based on its curved shape, which forms a substantial part of an ellipse. Thus, a simple and plausible interpretation of lane 2 is that it is a circular ring seen at an intermediate inclination. In Figure 11 we show a false-color F606W image of the central region of the nebula, with elliptical curves fitted (by eye) to the shapes of lanes 1 and 2. Henceforth, we will refer to the structures represented by lane 1 and lane 2 as torus 1 and torus 2, respectively.

The two dust lanes may also be interpreted as two parts of a single torus with an inhomogeneous structure. In this hypothesis (the "tortured-waist" hypothesis), the torus is substantially extended in latitude and has a large region in its middle (projected onto region M), which is significantly optically thin compared to regions lying along its top (northeast), bottom (southwest), and right-hand side (northwest) boundaries—these regions then manifest themselves as the two dark lanes on opposite sides of M. Thus, torus 1 and torus 2 are simply the densest parts of an overall toroidal structure. We discuss reasons in favor of and against each of the above hypothesis later (§ 11).

We derive rough estimates of the optical depth and mass of each torus[18] by assuming that the intrinsic background intensity obscured by them is equal to the average of the intensity on either side of each torus. Since there is significant uncertainty in fitting the background intensity which was done using a spline fit) because of the strong gradients in it across the tori, this procedure yields a 0.6 μm optical depth for torus 1 which is uncertain by a factor of ~ 2: the peak extinction optical depth is

---

[17] Not to be confused with the *very* fast (~ 1000 km s^{-1}), isotropic, radiative wind, which is believed to emanate from the hot central stars of planetary nebulae.

[18] These estimates do not depend significantly on which of the two interpretations for the dust lanes is correct.
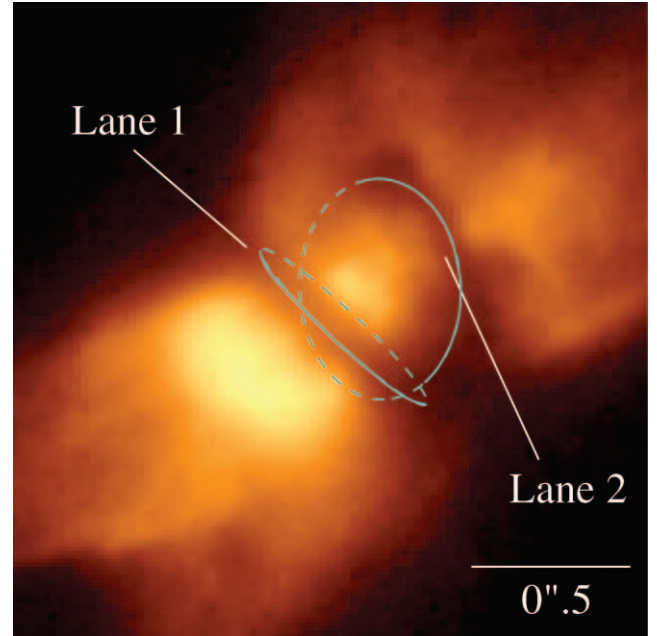

Fig. 11.—False-color (*log stretch*) F606W image of the central region of IRAS 19024+0044 showing lanes 1 and 2, and elliptical curves fitted (by eye) to their shapes. The solid (dashed) parts of the ellipses represent the foreground (background) parts of the dust lanes. The orientation of this image is identical to that in Figs. 1–4.

$\tau_{T1}(0.6\ \mu m) \sim 0.8$ from the F606W image, giving a mass surface density $\Sigma_{T1} = \tau_{T1}(0.6\ \mu m)/\kappa_a(0.6\ \mu m) \sim 7 \times 10^{-3}$ g cm^{-2}, where $\kappa_a(0.6\ \mu m) \sim 230/(g_d/100)$ cm^2 g^{-1} is the opacity (per unit mass of gas+dust) at 0.6 μm, based on models of observed interstellar medium (ISM) dust extinction properties (Whitney 1995) and scaled for the difference between the value of the gas-to-dust ratio for the ISM (100) and AGB mass-ejecta ($g_d \sim 200$; e.g., Knapp 1985). With a diameter for Torus 1 of $\phi_{T1} \sim 0\rlap{.}''7$ and a spatial width (FWHM) of $w_{T1} = 0\rlap{.}''16$ measured from the F606W image, we derive its total mass to be $\pi\phi_{T1}w_{T1}\Sigma_{T1} \sim 3.5 \times 10^{-3}(D/3.5\ \text{kpc})^2\ M_\odot$. We also find that $\tau_{T1}(0.8\ \mu m)$, derived from the F814W image, is comparable to $\tau_{T1}(0.6\ \mu m)$, although expected to be a factor 0.7 smaller, indicating that the dust grains are somewhat larger than typical ISM grains. Similarly, $\tau_{T1}(1.1\ \mu m)$, derived from the F110W image is ~ 0.5 (but the derivation is more uncertain because the absorption feature is weaker), significantly larger than the expected value, 0.35, obtained by scaling from $\tau_{T1}(0.6\ \mu m)$. The optical depth and mass of torus 2 are more uncertain (because it is less well delineated), but about a factor of 2 smaller, than that of Torus 1.

8. LOBES

In this section we derive key physical properties—optical depths, masses and expansion ages—of the lobes on the basis of their colors and sizes. The observed nebular colors result from the combined effect of reddening due to extinction and blueing due to scattering. For example, the average ratio of the 0.6 to 0.8 μm surface brightness in the lobes ranges from 0.8–1.2, compared to a value of 1.36 for the intrinsic starlight.

Using equation (1) of Sahai et al. (1999c) for the observed scattered light at any point in the nebula (setting $y = 1$), we can use the ratio of the surface brightnesses at any two wavelengths, λ_1 and λ_2 for interstellar extinction) at a representative point in the lobes to derive a radial extinction optical depth (τ_e) to, and a line-of-sight scattering optical depth (τ_s) at, that point. Taking
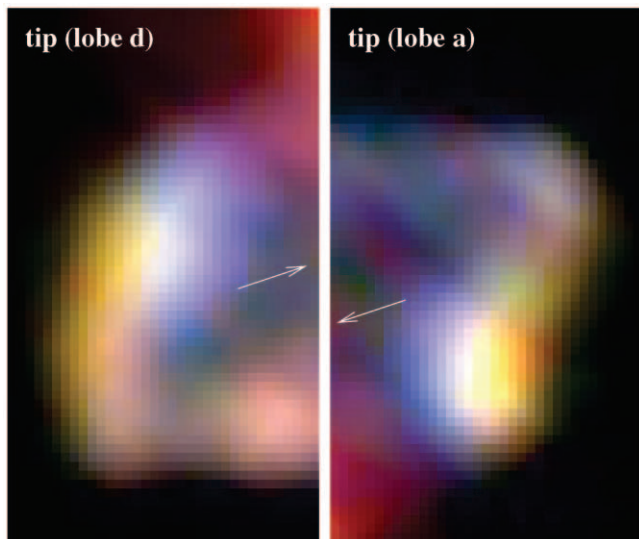
Fig. 12.—Color image of the tips of lobes d and a, made by combining the F606W (*blue*), F110W (*green*), and F160W (*red*) images. The vector in each panel points toward the center of the nebula. The orientation of these images is identical to that in Figs. 1–4.

Fig. 13.—Radial intensity cuts along the PA of the lobe pair a-d at 0.6 (*solid curve*) and 1.6 μm (*dash-dot curve*) generated from the F606W (ACS) and F110W (NICMOS) images showing the "layered" structure of the tips as a function of wavelength. The radially decreasing intensities have been multiplied by r^2 (the radial offset from the center) and scaled by arbitrary factors for easy comparison of the tip locations in the different cuts. [*See the electronic edition of the Journal for a color version of this figure.*]

such a point in lobe d, located at a radius 1″36 from the center, and $\lambda_1 = 0.6$, $\lambda_2 = 0.8$ μm, with corresponding fluxes 0.40 and 0.57 mJy arcsec^{-2}, respectively, we find $\tau_e(0.6$ μm$) = 1.5$ and $\tau_s(0.6$ μm$) = 0.04$. However, with these values of τ_e and τ_s, the predicted surface brightnesses at 1.1 and 1.6 μm are 0.47 and 0.18 mJy arcsec^{-2}, respectively, significantly lower than the observed ones, 0.87 and 0.70 mJy arcsec^{-2}. With $\lambda_1 = 0.6$ μm, if we use $\lambda_2 = 1.1$ μm, we find $\tau_e(0.6$ μm$) = 2.5$ and $\tau_s(0.6$ μm$) = 0.11$, but if $\lambda_2 = 1.6$ μm, then $\tau_e(0.6$ μm$) = 3.17$ and $\tau_s(0.6$ μm$) = 0.21$. This progressive increase in the derived optical depths at 0.6 μm with increasing λ_2 suggests that the "small-grain" scattering cross sections used in our derivation are too small at the longer wavelengths, and that larger values, implying larger grains, are required. We have checked that this result does not depend on our specific choice of the location in the lobes for which we have carried out the above analysis. In addition to our result in the previous section indicating large grains in I19024's central tori, similar or independent observational evidence for the presence of large grains in the dense central regions of several other protoplanetary nebulae has been found (e.g., AFGL 2688 [Sahai et al. 1998a, 1998b; Jura et al. 2000], IRAS 04296+3429 [Sahai 1999], and Red Rectangle [Jura et al. 1997]).

The bright, well-defined tips of lobes a and d show a "layered" brightness structure from short to long wavelengths (Fig. 12). Radial cuts of the intensities at different wavelengths show that the region of peak surface brightness moves outward in going from optical (e.g., 0.6 μm) to near-infrared (e.g., 1.6 μm) wavelengths (Fig. 13), implying that these regions are optically thick to the stellar radiation at 0.6 μm. Hence, by setting the 0.6 μm optical extinction in the tips to unity, we derive a minimum dust mass for each tip of about 1.2×10^{-5} $(D/3.5)^2$ $M_\odot$, assuming a circular shape for each tip with a diameter equal to its projected size, ∼0″5. If we assume a value of the gas-to-dust ratio, $g_d = 200$, typical of AGB mass ejecta, then the total mass of each tip is 2.5×10^{-3} $M_\odot$. Given that the total surface area of each lobe is about 10 times the area of each tip, and that the optical depths of other regions in the walls of the lobes are typically ∼0.1, we estimate that the total amount of mass in the lobe walls, summed over all the lobes, is $\gtrsim 0.02(D/3.5)^2$ $M_\odot$.
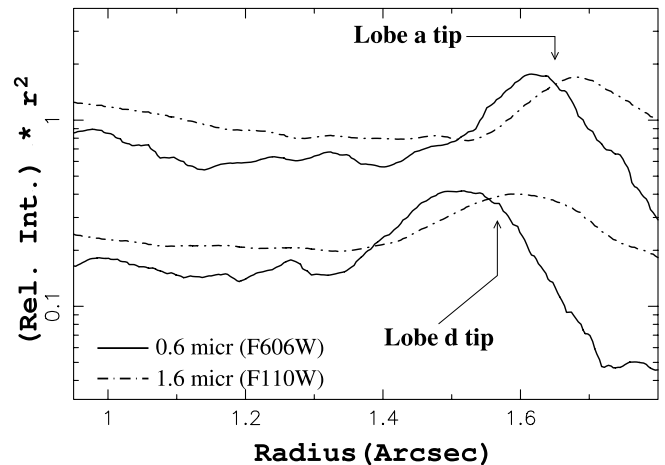
The true expansion age for the lobes ($t_{\rm exp}$) cannot be derived directly from the speed of the fast post-AGB outflows that created them (which we assume to be V_f, the velocity of the fast outflow described in § 6), but requires detailed hydrodynamic modeling of the interaction of these collimated flows with the progenitor AGB envelope. Such modeling, by Lee & Sahai (2003), shows that elongated lobes seen in PPNs are most likely "momentum-driven" shells (i.e., the dissipative hydrodynamic interaction of the fast outflow with its surroundings is fully radiative, preventing the build-up of thermal pressure and the inflation of large bubble-shaped shells). In their models, the ratio of the true expansion age to the "observed" one obtained by dividing the lobe length l by the fast wind speed V_f, is ∼1.8; if we adopt the same ratio for I19024, we find that the typical expansion age for a lobe is about 540 (100 km s^{-1}/V_f)(l/1.8″)(D/3.5 kpc) yr. However, since this ratio depends in detail on the relative momenta of the interacting winds, our estimate of $t_{\rm exp}$ is quite uncertain.

9. THE PROGENITOR AGB ENVELOPE

Faint nebulosity can be seen outside the lobe regions at intermediate and low latitudes and most likely represents the part of the progenitor AGB envelope that has not been significantly affected as yet by the processes which have formed the lobes. We have measured the radial profile of the 0.6 and 0.8 μm surface brightnesses using radial cuts generated from the F606W and F814W images (Fig. 14). In these cuts, the surface brightness has been averaged over large angular ranges (which avoid the lobes)— 80° in the southeast quadrant, and 40° in the northwest quadrant—in order to increase the S/N in the very faint outer regions. These angular regions were selected to avoid the presence of bright field stars, which contribute a significant amount of scattered light around them.

We find that the surface brightness, both at 0.6 and 0.8 μm, varies as $r^{-\alpha}$, with $\alpha \sim 3.2 \pm 0.2$, in the "halo" region ($r \gtrsim 0″6$). Note that the direct illuminating source for the halo regions in the cuts is not the central star, but the bright central region of the nebula (a combination of the anvil and feature M). The uncertainty in the exponent is largely due to the fact that the effective center of this illuminating source cannot be precisely determined.
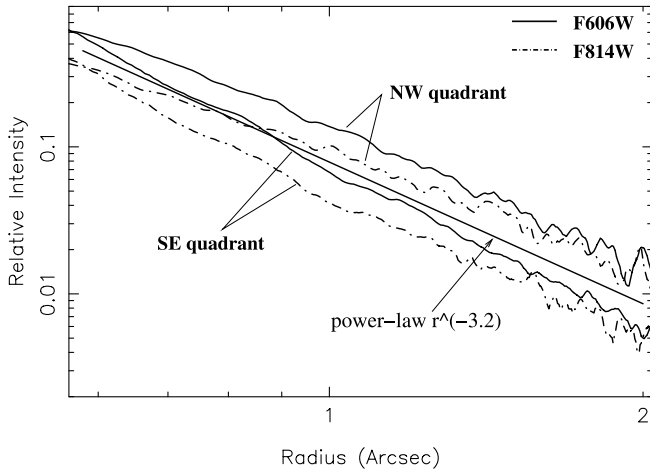
Fig. 14.—Radial profiles of halo surface brightness at 0.6 (*solid curve*) and 0.8 μm (*dash-dot curve*) generated from the F606W and F814W images. The surface brightness has been averaged over large angular ranges that avoid the nebular lobes (80° in the southeast quadrant, and 40° in the northwest quadrant) in order to increase the S/N in the very faint outer regions of the halo. A radial power law, with exponent −3.2, is shown for comparison. [*See the electronic edition of the Journal for a color version of this figure.*]

The halo extends to a radius of about 2″ or $10^{17}(D/3.5 \text{ kpc})$ cm, where it becomes limited by uncertainties in the background sky level. The observed value of α in the halo is consistent with $\alpha \sim 3$, which characterizes the scattered light distribution of an optically thin spherical nebula with an inverse-square radial density (e.g., resulting from a constant mass-loss at a constant expansion velocity). The size of the halo implies that the dense mass-loss phase of I19024's AGB progenitor lasted for at least 2600 (13.6 km s^{-1}/$V_{e,\text{agb}}$)(D/3.5 kpc) yr.

10. MOLECULAR GAS AND DUST

In this section we set constraints on the total mass of molecular gas and dust in I19024 and its luminosity. The far-infrared fluxes of I19024 indicate the presence of a large mass of cool (~100 K) dust in the nebula. We have fitted I19024's color-corrected *IRAS* fluxes (3.1, 52.5, 36.3, and 14.6 Jy at 12, 25, 60, and 100 μm, respectively) and the *MSX* fluxes (0.68, 2.6, 8.4, and 32.6 Jy at 8.8, 12.1, 14.7, and 21.7 μm, respectively) using a multicomponent model (Sahai et al. 1991) (Fig. 15). We have also retrieved the *IRAS* LRS spectrum of I19024 (also shown in Fig. 15) but have not used it to constrain the model because of its relatively low S/N. The overall photometry of the long-wavelength portion (10.5–22.5 μm) of the LRS spectrum is somewhat lower than that indicated by the broadband fluxes in this wavelength region. Assuming power-law (λ^{-p}, with $p = 1$) dust emissivity with a value of 150 cm^2 g^{-1} (per unit *dust* mass) at 60 μm (Jura 1986), our best-fit model requires "cool" (109 K) and "warm" (280 K) dust in components of mass $M_{d1} = 5.7 \times 10^{-4}$ and $M_{d2} = 1.5 \times 10^{-7}$ $M_\odot$ (the masses scale as D^2). Our model produces a good fit to the overall slope exhibited by the long-wavelength portion (10.5–22.5 μm) of the LRS spectrum and predicts a $\lambda = 2.6$ mm continuum flux of 1.4 mJy, consistent with our observed upper limit. The total luminosity of I19024 is estimated to be 2850 $(D/3.5)^2$ $L_\odot$ from our model fit to the observed spectral energy distribution.

We have estimated the mass in the molecular envelope of IRAS 19024 from the integrated CO 1–0 profile assuming that the line is optically thin (a lower limit to the mass is obtained if the CO 1–0 line is optically thick). The CO excitation is described
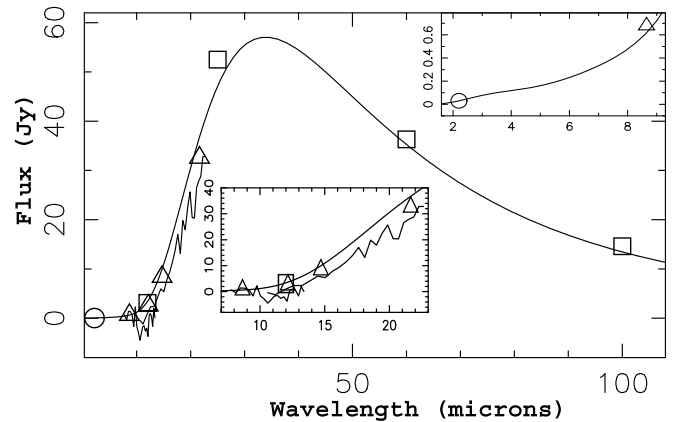

Fig. 15.—Observed and model infrared fluxes of IRAS 19024+0044. Observations: IRAS LRS spectra, *ragged curves*. Photometric data: K band, *circle* (Garcia-Lario et al. 1997); *MSX*, *triangles*; *IRAS*, *squares*. Model: *smooth curve*. Insets show expanded views of selected wavelength regions. [*See the electronic edition of the Journal for a color version of this figure.*]

by a rotational temperature that it is assumed to be similar to the kinetic temperature, T_{kin}; i.e., we are assuming the CO lines to be thermalized. This is a reasonable approximation for most PPNs, which usually have densities larger than the CO 1–0 critical density ($\approx 10^3$ cm^{-3}) in most regions of their envelopes. Adopting a $T_{\text{kin}} = 10$ K and a relative CO-to-H$_2$ abundance of 2×10^{-4}, which are common values in PPNs (Bujarrabal et al. 2001 and references therein), and the well-known molecular parameters of CO (e.g., Rohlfs & Wilson 2000), we derive a molecular mass, $M_g = 0.025(D/3.5 \text{ kpc})^2$ $M_\odot$. Since the CO emission source is unresolved or marginally resolved, we estimate its spatial extent to be 4″.5 (geometric mean of the major and minor axis of the beam), to derive an expansion age, $t_{\text{exp}} \lesssim 2870(D/3.5 \text{ kpc})$ yr and a mass-loss rate $\gtrsim 9 \times 10^{-6}(D/3.5 \text{ kpc})$ $M_\odot$ yr^{-1}.

The derived mass and mass-loss rate are likely to be lower limits since the emission is most likely optically thick, and the kinetic temperature significantly lower than 10 K, and probably close to the microwave background temperature (2.73 K), throughout much of the envelope. For example, with $T_{\text{kin}} = 3$ K, the derived mass $M_g = 0.11$ $M_\odot$, a factor 4.5 times larger than the value derived above; at such low temperatures the derived mass shows a very strong nonlinear dependence on T_{kin}. Low kinetic temperatures could result from the fact that the main source of heating of molecular gas in AGB circumstellar envelopes— frictional heating by dust grains drifting through the gas due to radiation pressure—is very weak in post-AGB objects like I19024, where there is a significant lack of short-wavelength (~1 μm) radiation reaching the outer regions of the envelope. For example, the ratio $\nu F_\nu / F_{\text{bol}}$ at 1 μm is 6.5×10^{-3} in I19024 but is 0.29 and 0.21, respectively, in the oxygen-rich AGB stars IK Tau and TX Cam. Although a significantly larger fraction of short-wavelength radiation does escape along directions within the solid angle subtended by the lobes (Ω_{lobe}) compared to that subtended by the nonlobe regions (Ω_{nlb}), it is likely that the fraction of molecular material in the envelope encompassed within Ω_{nlb} is much larger than that within Ω_{lobe} for the following reasons. First, the observed CO spectrum does not show any significant high-velocity emission, providing observational support for the relative lack of molecular material within or at the tips of the lobe regions.

Second, Ω_{nlb} encompasses low-latitude regions which, as indicated by the presence of lanes 1 and 2, appear to have enhanced densities, and third, Ω_{nlb} is significantly larger than Ω_{lobe}. On the basis of our independent gas and dust mass measurements,

we derive a minimum gas-to-dust ratio, $g_d = 44$, which is significantly lower than the typical value of 200 found for the circumstellar envelopes of AGB stars; and we conclude that this is (at least partially) because the molecular mass has been underestimated.

11. DISCUSSION: THE STRUCTURE AND FORMATION OF I19024

Our detailed study of I19024 has important implications for current models for producing aspherical PNs. Axisymmetric bipolar shapes can, in principle, be produced by the generalized interacting stellar winds (GISW) model, in which a very fast, radiatively driven, isotropic post-AGB stellar wind is hydrodynamically collimated by an AGB CSE assumed to be equatorially dense (Balick & Frank 2002). However, considerable observational evidence has recently accumulated that indicates that the fast wind, which is responsible for the shaping, is (1) intrinsically collimated (Sahai 2002) and (2) not radiatively driven (Bujarrabal et al. 2001). On the basis of their imaging survey of young PNs, Sahai & Trauger (1998) hypothesized that collimated fast winds are the primary mechanism for the dramatic change in circumstellar geometry and kinematics as stars evolve off the AGB.

The presence of (1) multiple elongated lobes in I19024 (for which the identity as a young preplanetary nebula has been established by our optical spectroscopy) and their highly-structured morphology, and (2) a fast (100 km s^{-1}) post-AGB outflow, provides general support for this hypothesis. I19024's multipolar morphology is remarkably similar to that of the "Starfish Twins," two very young planetary nebulae (Sahai 2000). Our imaging of I19024 indicates that such starfish morphologies[19] are already well established during the preplanetary nebula phase, and therefore, that a very fast radiative wind from, and/or photoionization by, the central star when it becomes sufficiently hot at the later PN evolutionary phase, does not play a major role in the nebular shaping process.

Can the starfish-like morphology observed in I19024 and several other objects[20] in the preplanetary or planetary nebula phase be understood in the context of physical mechanisms for producing collimated outflows? Most of these rely on the presence of an accretion disk that powers a jetlike outflow; a wobble in the disk, e.g., due to radiative instabilities, can cause the axis of the jetlike outflow to change direction (Livio & Pringle 1997). A precessing bipolar jet, in which the fast outflow is in the form of discrete blobs ejected in discontinuous episodes, could also lead to multiple lobes in different directions. We note that the detailed point-symmetric structure matching between the tips of lobes a and d in I19024 suggests that the collimated outflow that produced these lobes must have changed its axis during its operation, although by much less than the angular separation between lobes. These compressed layers in the lobe tips are similar to the ansae seen in other PPNs and PNs. The absence of such features at the ends of other lobes suggests that they do not have currently active jets, allowing the presumably once-compressed layers at the lobe tips to rebound or expand in the absence of recent ram pressure. A sensitive search for emission lines

in I19024 should be made in order to test these expectations for the presence and absence of currently active shocks in its lobes.

But the main difficulty encountered by the hypothesis of a direction-changing bipolar jet in explaining objects with starfish morphology is that the different lobes appear to have very similar lengths, and therefore, in all likelihood, similar expansion ages, which presumably require the operation of several collimated fast outflows in near-simultaneity in different directions. Thus, in I19024, if the jet axis wobbled, for example, from the P.A. for lobes c and f, to lobes b and e, to lobes a and d, then one would expect the c and f lobes to be longest, b and e shorter, and a and d shortest. This is because after the jet switches direction from one lobe pair to the next, we expect the expansion of the dense walls of the first lobe pair not to slow down significantly until they have dissipated their excess momentum by sweeping up enough ambient gas. However, because of the rapidly decreasing (r^{-2}) density of the ambient gas, such slowing down may not be effective. Numerical simulations are sorely needed to quantitatively investigate whether or not the starfish morphology can be generated with a bipolar jet that changes its direction. If such simulations are unsuccessful, we may well have to consider more exotic ideas such as the "explosive" ejection of matter along different directions driven by a correspondingly fast release of magnetic energy from the central star.

Nevertheless, we can claim to have made some progress in understanding the shaping of bipolar planetary nebulae as a process which can be initiated by the operation of collimated fast winds during the preplanetary phase, or even earlier, i.e., during the late AGB phase (Sahai & Trauger 1998; Soker & Rappaport 2000; Sahai 2002). But the origin of the dense waists in these objects remains a mystery. Until very recently, the waist was simply envisaged as an equatorial/low-latitude region of enhanced density. Although Bondi-Hoyle accretion of the AGB wind by a close ($\lesssim 10-20$ AU) companion can produce a small disk, with a size of up to the binary separation (Morris 1990; Mastrodemos & Morris 1998), the large observed sizes of the waist structures ($\sim 10^{16}$ cm) rule out the possibility that these are accretion disks. Most likely, mechanisms to explain the waist region need to produce enhanced mass loss in the equatorial plane over an extended period of time (several 100 yr), e.g., from cool magnetic spots near the star's equatorial plane (Soker 1998).

More recently, Soker & Rappaport (2000, hereafter SK00) have suggested that the compression of the AGB wind toward the equatorial plane by a fast wind inflating large polar lobes can also produce a dense waist.[21]

Can such mechanisms explain the simultaneous presence of two dust lanes (lanes 1 and 2) in the central region of I19024? The answer to this question depends on our interpretation of the dust lanes but, unfortunately our current data set does not allow a strong preference for either the two-tori or the tortured-waist interpretation. Lobes in bipolar PPN are expected,[22] and generally observed, to emanate from the two sides of the central waist. Thus, in I19024, if lane 1 and lane 2 were part of a wide torodial waist structure (defining its northeast and southwest boundaries), one would expect to see the south-facing (north-facing) edge of lobe c (a) to terminate at lane 2, and the east-facing (north-facing)

---

[19] The label "starfish" is based on the two-dimensional projected shape on the sky and is not meant to imply that the three-dimensional nebular structure is similar to the somewhat planar structure of a real starfish—in fact, it is quite likely that the axes of the multiple lobes do not lie in a plane.

[20] The well-studied PPN, CRL 618 (e.g., Trammell & Goodrich 2002; Sánchez Contreras et al. 2002), although not labeled as such, also belongs to the starfish class.

[21] A plausible example of a PPN which may have undergone such a process, based on its morphology, is IRAS 09371+1212, or Frosty Leo, which shows two prominent inflated lobes and a dense waist (Sahai et al. 2000a).

[22] From theories both in which the waist is a product of lobe formation via the SK00 compression process, or represents a preexisting structure which collimates a fast outflow to produce a bipolar PPN (GISW model).

edge of lobe d (f) to terminate at lane 1—this overall pattern is not observed. In fact, the optical images show that the boundaries of lobes c and d meet in a V-shaped vertex, which defines the southeast limit of lane 1, supporting the idea that lane 1 forms the canonical dense waist seen in bipolar PPNs (and therefore lane 2 is an independent geometrical structure). However, such a distinct vertex between lobes a and f is not clearly seen on the northwest side of the nebula; the morphology of the central region there appears consistent with the idea that lobes a and f emanate from a wide torus.

Theoretically, in the tortured-waist interpretation of the dust lanes, the proposed inhomogeneity could result from the action of a fast low-latitude outflow (e.g., like the ones found in the waists of the bipolar PPNs AFGL 2688 and IRAS 09371+1212 [Sahai et al. 1998a, 2000a; Cox et al. 2000]) excavating large parts of a geometrically wide torus. But this explanation appears rather contrived, because it requires the excavation process to clear out a very specific central part of the torus, leaving thin extended regions at its edges (which form the dust lanes) intact. Such an excavation would hardly appear to be the normal outcome of the operation of the type of multiple low-latitude outflows seen in AFGL 2688 and IRAS 09371+1212. If, however, we accept the alternative "two-tori" hypothesis that the dust lanes are two tori inclined to each other, we do not have a good theoretical explanation for how they are formed. It is difficult to imagine how the SK00 mechanism could produce two inclined tori, and furthermore, since the lobes in I19024 appear to be highly collimated, momentum-driven shells, it appears unlikely that they can provide sufficient compression of the AGB wind toward the equator for the SK00 model to work.

But although (at present) it appears easier to explain the tortured-waist picture rather than the two-tori picture of the dust lanes, this is not sufficient grounds to reject the two-tori hypothesis because *HST* imaging shows complex structures in the waists of several other evolved objects besides I19024 for which we do not, as yet, have any theoretical explanation. The waists of several young PNs, which are sufficiently tilted away from an edge-on configuration, reveal a variety of puzzling geometrical structures. For example, He 2−47 (one of the Starfish Twin PNs), has two point-symmetrically located, probably coplanar, partial rings (Sahai 2000). He 2−113 shows two noncoplanar, but coaxial, knotty rings, which are not orthogonal to the general bipolar axis of this PN (Sahai et al. 2000). In the Etched Hourglass Nebula MyCn 18, the waist consists of a bright outer ring coaxial with the hourglass axis, together with a smaller inner ring whose axis appears to be orthogonal (in projection) to that of the outer ring (Sahai et al. 1999a). In the above three objects, we have also noted that the central star appears to be offset from the centers of the different geometrical structures defining, or within, the waist. In I19024, the central star is not seen, but it appears plausible that it lies close to peak P. In the two-tori interpretation, the full extent and curvature of the two tori are not sufficiently well-defined to allow us to determine their geometrical centers with enough precision for comparison with P's location. In the tortured-waist interpretation, P lies roughly in the middle of the waist as expected.

We have derived the masses of different structural components of the nebula from the optical images, as well as total molecular and dust masses in the nebula, respectively, from model fits to the CO $J = 1-0$ and far-infrared fluxes. We have offered these mass estimates because they are valuable for developing and constraining theoretical models for nebulae such as I19024—for example, numerical simulations of collimated, fast outflows interacting with the progenitor AGB envelope for lobe produc-tion (e.g., Lee & Sahai 2003). Our estimates of the total nebular mass are small compared to the mass expected to be ejected ($\gtrsim 0.5$) by a star with a main-sequence mass of $\gtrsim 1 \; M_\odot$, before it becomes a white dwarf, and hence we cannot set useful constraints on the initial mass of the central star of I19024 from our mass estimates. However, we have noted earlier (§ 5.1) that comparing I19024's luminosity with predictions from stellar evolutionary tracks indicates that the initial mass of I19024 is likely to be relatively low, $\sim 1-1.5 \; M_\odot$. The largest nebular mass of I19024 is in the molecular component—the value we derive from the CO data, $0.025 \; M_\odot$, is most likely an underestimate (§ 10). We do not know as yet what fraction of the mass in the lobes ($\sim 0.02 \; M_\odot$) or tori ($\sim 0.005 \; M_\odot$) is molecular—this can only be established with interferometric observations of CO in I19024 with much better angular resolution and dynamic range than available in our current data. If we scale the mass of the cool dust component derived from the far-infrared fluxes using a gas-to-dust ratio of 200, we obtain $0.1 \; M_\odot$, which may be more representative of the nebular mass. Note that it is intrinsically difficult to detect all of the mass that has been ejected by the central star while on the AGB. For a fixed rate of AGB mass-loss at a constant outflow velocity, the total mass of the circumstellar envelope is proportional to its size. But the radius of an envelope detected via CO observations is limited by photodissociation (due to the interstellar ultraviolet radiation field) to few times 10^{17} cm for a mass-loss rate of $\sim 10^{-5} \; M_\odot \; \mathrm{yr}^{-1}$ (Mamon et al. 1988), limiting the detectable mass to $\lesssim 0.1 \; M_\odot$; insufficient excitation may restrict the detectable envelope radius (and thus mass) to even smaller values. Only very sensitive long-wavelength (e.g., $200-800 \; \mu$m) observations of dust emission can probe material at larger radii.

12. CONCLUSIONS

Using *HST*'s ACS and NICMOS instruments, we have imaged the OH/IR star I19024 at optical and near-infrared wavelengths (using broadband filters at 0.6, 0.8, 1.1, and 1.6 μm) during our surveys of candidate preplanetary nebulae. Optical spectroscopy and millimeter-wave (interferometric) mapping of its molecular line emission has been carried out from ground-based facilities. We find the following:

1. I19024 is a multipolar nebula of size $\sim 3\farcs7 \times 2\farcs3$, with at least six elongated lobes emanating from the center of the nebula. Two of the lobes show limb-brightened tips, whose structure is point-symmetric about the location of a central intensity peak in the longest-wavelength (1.6 μm) image. This intensity peak is most likely located at or close to the central star, which is not seen directly in the images. The central region of the nebula shows two dark dust lanes, which may be either two inclined dusty toroidal structures, or the dense parts of a single wide, inhomogeneous, toroid.

2. A very faint, surface brightness–limited, diffuse halo surrounds the lobes. This halo has a power-law radial surface-brightness profile with an exponent of about −3 and most likely represents the remnant spherical circumstellar envelope formed as a result of constant mass-loss during the AGB phase over the past several thousand years.

3. Long-slit/echelle optical spectroscopy shows a fairly red, relatively featureless continuum spectrum, which (after correcting for reddening) is consistent with a G5–G0 spectral type for the central star, thus confirming I19024's identity as a preplanetary nebula. The source has a spatially compact source of Hα and Hβ emission; the Hα and Hβ lines show an intense, narrow central core with very broad weak wings and a narrower blue-shifted absorption feature. The latter indicates the presence of a fast post-AGB outflow with a speed of about 100 km s^{-1}.

4. The CO $J = 1-0$ line emission, with size (FWHM) $5\rlap{.}''5 \times 4\rlap{.}''4$, is marginally resolved along the minor axis of the elliptical beam. The integrated $J = 1-0$ line profile is centered at $V_{lsr} = 50$ km s^{-1}, and the expansion velocity of the molecular envelope, derived as half the full-width at zero intensity of the line, is 13 km s^{-1}. No continuum was detected at 2.6 mm to a 3 σ limit of 6 mJy.

5. The kinematic distance to I19024, based on its radial velocity, is 3.5 kpc. The bolometric flux is 7.3×10^{-9} ergs s^{-1} cm^{-2}, and the luminosity 2850 $L_\odot$. The relatively low luminosity, in comparison with stellar evolutionary models, indicates that the initial mass of the central star was $\sim 1-1.5$ $M_\odot$.

6. We have derived the masses of different structural components of the nebula from the optical images, as well as total molecular and dust masses in the nebula. The lobes, which appear to be hollow structures with dense walls, have a total mass greater than or equal to about 0.02 $M_\odot$. The dusty tori in the center have masses of few times 10^{-3} $M_\odot$. From modeling the *IRAS* and *MSX* fluxes, we find that I19024 has cool (109 K) and warm (280 K) components of dust mass 5.7×10^{-4} and 1.5×10^{-7} $M_\odot$. From the observed CO $J = 1-0$ line flux, we derive a molecular mass $\gtrsim 0.025$ $M_\odot$, which is likely to be an underestimate, and from the spatial extent of the CO emission, we derive an expansion age $\lesssim 2870$ yr and a mass-loss rate $\gtrsim 10^{-5}$ $M_\odot$ yr^{-1}.

7. Although collimated fast outflows (produced, e.g., by an accretion disk around a binary companion) can explain the formation of individual lobe pairs, the presence of multiple lobes with similar sizes and (presumably) expansion ages in I19024 and other starfish nebulae like it are hard to understand. The presence of two dust lanes, which may be either two inclined dusty toroidal structures or the dense parts of a single wide, inhomogeneous, toroid, is also not well understood.

In summary, our study of I19024 has revealed the detailed structure of a preplanetary nebula that cannot be understood in its entirety within the context of current theoretical models, even those that admit the complexity of a binary companion and an associated, wobbling/precessing accretion disk powering a fast, collimated, episodic outflow. We expect that I19024, in particular, and other "starfish" nebulae in general, will provide strong impetus and inspiration for the development of new theoretical models for understanding how planetary nebulae are formed from AGB stars.

REFERENCES

Allen, D. A., Hyland, A. R., & Caswell, J. L. MNRAS, 1980, 192, 505
Balick, B., & Frank, A. 2002, ARA&A, 40, 439
Bowers, P. F., Johnston, K. J., & Spencer, J. H. 1983, ApJ, 274, 733
Bujarrabal, V., Castro-Carrizo, A., Alcolea, J., & Sánchez Contreras, C. 2001, A&A, 377, 868
Cox, P., Lucas, R., Huggins, P. J., Forveille, T., Bachiller, R., Guilloteau, S., Maillard, J. P., & Omont, A. 2000, A&A, 353, L25
Garcia-Lario, P., Manchado, A., Pych, W., & Pottasch, S. R. 1997, A&AS, 126, 479
Goodrich, R. W. 1991, ApJ, 376, 654
Gottlieb, E. W., & Liller, W. 1976, ApJ 207, L135
Hakkila, J., Myers, J. M., Stidham, B. J., & Hartmann, D. H. 1997, AJ, 114, 2043
Hrivnak, B. J., Kwok, S., & Su, K. Y. L. 1999, ApJ, 524, 849
Jura, M. 1986, ApJ, 303, 327
Jura, M., Turner, J. L., & Balm, S. P. 1997, ApJ, 474, 741
Jura, M., Turner, J. L., Van Dyk, S., & Knapp, G. R. 2000, ApJ, 528, L105
Knapp, G. R. 1985, ApJ, 293, 273
Kwok, S., Hrivnak, B. J., & Su, K. Y. L. 2000, ApJ, 544, L149
Lee, C.-F., & Sahai, R. 2003, ApJ, 586, 319
Livio, M., & Pringle, J. E. 1997, ApJ, 486, 835
Mamon, G. A., Glassgold, A. E., & Huggins, P. J. 1988, ApJ, 328, 797
Mastrodemos, N., & Morris, M. 1998, ApJ, 497, 303
Morris, M. 1987, PASP, 99, 1115
———. 1990, in From Miras to Planetary Nebulae: Which Path for Stellar Evolution?, ed. M. O. Mennessier & A. Omont (Paris: Editions Frontières), 520
Morris, M., Sahai, R., Claussen, M. 2003, Rev. Mexicana Astron. Astrofis. Ser. Conf., 15, 20
Neri, R., Kahane, C., Lucas, R., Bujarrabal, V., & Loup, C. 1998, A&AS, 130, 1
Riera, A., Garcia-Lario, P., Manchado, A., Pottasch, S. R., & Raga, A. C. 1995, A&A, 302, 137
Rohlfs, K., & Wilson, T. L. 2000, Tools of Radio Astronomy, ed. K. Rohlfs & T. L. Wilson (New York: Springer, 2000)
Sahai, R. 1999, ApJ, 524, L125
———. 2000, ApJ, 537, L43
———. 2002, Astron. Space. Sci. Lib., 265, 53

Sahai, R. 2004, in ASP Conf. Ser. 313, Asymmetrical Planetary Nebulae III, ed. M. Meixner et al. (San Francisco: ASP), 114
Sahai, R., Bujarrabal, V., Castro-Carrizo, A., & Zijlstra, A. 2000a, A&A, 360, L9
Sahai, R., Bujarrabal, V., & Zijlstra, A. 1999a, ApJ, 518, L115
Sahai, R., Hines, D. C., Kastner, J. H., Weintraub, D. A., Trauger, J. T., Rieke, M. J., Thompson, R. I., & Schneider, G. 1998a, ApJ, 492, L163
Sahai, R., Nyman, L.-Å., & Wootten, A. 2000b, ApJ, 543, 880
Sahai, R., & Sánchez Contreras, C. 2004, in ASP Conf. Ser. 313, Asymmetrical Planetary Nebulae III, ed. M. Meixner et al. (San Francisco: ASP), 32
Sahai, R., Te Lintel Hekkert, P., Morris, M., Zijlstra, A., & Likkel, L. 1999b, ApJ, 514, L115
Sahai, R., & Trauger, J. T. 1998, AJ, 116, 1357
Sahai, R., Wootten, A., Schwarz, H. E., & Clegg, R. E. S. 1991, A&A, 251, 560
Sahai, R., Zijlstra, A., Bujarrabal, V., & Te Lintel Hekkert, P. 1999c, AJ, 117, 1408
Sahai, R., Zijlstra, A., Sánchez Contreras, C., & Morris, M. 2003, ApJ, 586, L81
Sahai, R., et al. 1998b, ApJ, 493, 301
Sánchez Contreras, C., & Sahai, R., 2001, ApJ, 553, L173
Sánchez Contreras, C., Sahai, R., & Gil de Paz, A. 2002, ApJ, 578, 269
Sánchez Contreras, C., Sahai, R., Gil de Paz, A., & Goodrich, R. W. 2003, BAAS, 35, 1220
Sevenster, M. N., van Langevelde, H. J., Moody, R. A., Chapman, J. M., Habing, H. J., & Killeen, N. E. B. 2001, A&A, 366, 481
Soker, N. 1998, MNRAS, 299, 1242
Soker, N., & Rappaport, S. 2000, ApJ, 538, 241
Thomas, R. M., Morton, D. C., & Murdin, P. G. 1979, MNRAS, 1888, 19
Trammell, S. R., & Goodrich, R. W. 2002, ApJ, 579, 688
Ueta, T., Meixner, M., & Bobrowsky, M. 2000, ApJ, 528, 861
van de Steene, G. C., Wood, P. R., & van Hoof, P. A. M. 2000, in ASP Conf. Ser. 199, Asymmetrical Planetary Nebulae II, ed. J. H. Kastner, N. Soker, & S. Rappaport (San Francisco: ASP), 191
Vassiliadis, E., & Wood, P. R. 1994, ApJS, 92, 125
Whitney, B. 1995, Rev. Mexicana Astron. Astrofis. Conf. Ser., 1, 201
Whittet, D. C. B. 1992, Dust in the Galactic Environment (Bristol: IPP), 67